

Effect of cationic order–disorder on the transport properties of $\text{LaBaCo}_2\text{O}_{6-\delta}$ and $\text{La}_{0.5}\text{Ba}_{0.5}\text{CoO}_{3-\delta}$ perovskites

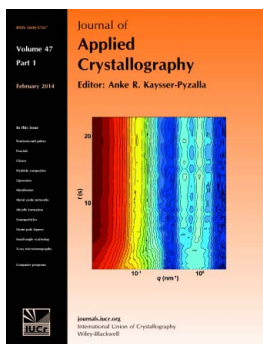
Diana Garcés, Cristian F. Setevich, Alberto Caneiro, Gabriel Julio Cuello and Liliana Mogni

J. Appl. Cryst. (2014). **47**, 325–334

Copyright © International Union of Crystallography

Author(s) of this paper may load this reprint on their own web site or institutional repository provided that this cover page is retained. Republication of this article or its storage in electronic databases other than as specified above is not permitted without prior permission in writing from the IUCr.

For further information see <http://journals.iucr.org/services/authorrights.html>



Many research topics in condensed matter research, materials science and the life sciences make use of crystallographic methods to study crystalline and non-crystalline matter with neutrons, X-rays and electrons. Articles published in the *Journal of Applied Crystallography* focus on these methods and their use in identifying structural and diffusion-controlled phase transformations, structure-property relationships, structural changes of defects, interfaces and surfaces, *etc.* Developments of instrumentation and crystallographic apparatus, theory and interpretation, numerical analysis and other related subjects are also covered. The journal is the primary place where crystallographic computer program information is published.

Crystallography Journals **Online** is available from journals.iucr.org

Effect of cationic order–disorder on the transport properties of $\text{LaBaCo}_2\text{O}_{6-\delta}$ and $\text{La}_{0.5}\text{Ba}_{0.5}\text{CoO}_{3-\delta}$ perovskites

Diana Garcés,^a Cristian F. Setevich,^b Alberto Caneiro,^c Gabriel Julio Cuello^d and Liliana Mogni^{c*}

^aCentro Atómico Bariloche, Instituto Balseiro–CNEA, Avenida Bustillo 9500, San Carlos de Bariloche, Rio Negro, 8400, Argentina, ^bDepartamento de Física, Universidad Nacional del Sur, Instituto de Física del Sur, Avenida Alem 1253, Bahía Blanca, Buenos Aires, 8000, Argentina, ^cCentro Atómico Bariloche, Instituto Balseiro–CNEA–CONICET, Avenida Bustillo 9500, San Carlos de Bariloche, Rio Negro, 8400, Argentina, and ^dDiffraction Group, Institut Laue–Langevin, 6 rue Jules Horowitz, BP 156, Grenoble, Isère, 38000, France. Correspondence e-mail: mogni@cab.cnea.gov.ar

A-site cationic ordered $\text{LaBaCo}_2\text{O}_{6-\delta}$ and disordered $\text{La}_{0.5}\text{Ba}_{0.5}\text{CoO}_{3-\delta}$ perovskite phases were obtained by solid state reaction. Their structural properties were studied at room temperature and 673 K, by combining powder diffraction techniques, X-ray diffraction and neutron powder diffraction with an independent determination of the oxygen content of the samples by thermogravimetry. $\text{La}_{0.5}\text{Ba}_{0.5}\text{CoO}_{3-\delta}$ exhibits cubic symmetry with cations randomly distributed, whereas $\text{LaBaCo}_2\text{O}_{6-\delta}$ shows tetragonal symmetry with the La^{3+} and Ba^{2+} ions distributed in alternating layers. The diffraction data were analyzed using the Rietveld method and different structural and microstructural models. Bond valence and Fourier methods were used to determine bond distances and neutron/electron density maps. $\text{LaBaCo}_2\text{O}_{6-\delta}$ exhibits a higher concentration of oxygen vacancies than $\text{La}_{0.5}\text{Ba}_{0.5}\text{CoO}_{3-\delta}$, because the O atom is weakly bonded to the LaO layers. The anisotropic atomic displacement and the neutron density distribution suggest a two-dimensional O-migration path for $\text{LaBaCo}_2\text{O}_{6-\delta}$ and a three-dimensional path for $\text{La}_{0.5}\text{Ba}_{0.5}\text{CoO}_{3-\delta}$. The mechanism of electrical conductivity is *via* electron holes with high mobilities ($\mu^{\text{La}_{0.5}\text{Ba}_{0.5}\text{CoO}_{3-\delta}} = 2.49 \text{ cm}^2 \text{ V}^{-1} \text{ s}^{-1}$ and $\mu^{\text{LaBaCo}_2\text{O}_{6-\delta}} = 1.48 \text{ cm}^2 \text{ V}^{-1} \text{ s}^{-1}$ at room temperature) and low activation energy ($E_a^{\text{LaBaCo}_2\text{O}_{6-\delta}} = 0.019 \text{ eV}$ and $E_a^{\text{La}_{0.5}\text{Ba}_{0.5}\text{CoO}_{3-\delta}} = 0.030 \text{ eV}$). It has also been found that the higher electronic and ionic conductivities in $\text{La}_{0.5}\text{Ba}_{0.5}\text{CoO}_{3-\delta}$ compared to those in $\text{LaBaCo}_2\text{O}_{6-\delta}$ are due to the higher dimensionality of transport and to greater overlapping between the Co 3d and O 2p orbitals.

© 2014 International Union of Crystallography

1. Introduction

In the past few years, cobaltites with perovskite structure and the related layered perovskites have been proposed as materials for high- and intermediate-temperature electrochemical devices.

This kind of material is attractive because of the presence of mixed ionic and electronic conductivities. The use of cobaltites with mixed conductivity as oxygen electrodes allows the oxygen reaction zone to be increased beyond the triple phase boundary, gas/electronic conductor/ionic conductor, to a gas/mixed conductor interface. Thus, $(\text{La,Sr})\text{CoO}_{3-\delta}$ (Teraoka *et al.*, 1988; Tai *et al.*, 1995), $(\text{Ba,Sr})\text{CoO}_{3-\delta}$ (Zhou *et al.*, 2009) and $(\text{La,Ba})\text{CoO}_{3-\delta}$ (Ishihara *et al.*, 2002; Setevich *et al.*, 2012) perovskites have been proposed for replacing the traditional pure electronic conductor as cathode in solid oxide fuel cells (SOFCs), owing to their low electrode polarization resistance

and their high power density. Furthermore, the surface exchange properties together with their high oxygen ionic conductivity make these materials suitable as oxygen exchange membranes (Petric *et al.*, 2000).

In the same way as perovskites are attractive for electrochemical application, the layered perovskites $\text{LnBaCo}_2\text{O}_{6-\delta}$ (Ln = lanthanide) are also interesting for this kind of application. These materials also show high rates of oxygen surface exchange (Tarancón *et al.*, 2007) and diffusivity (Kim *et al.*, 2009), which combined with their high electrical conductivity (Zhang *et al.*, 2008; Kim *et al.*, 2008) make them potential materials for oxygen separation membranes (Kim *et al.*, 2009; Zhang *et al.*, 2008) and intermediate-temperature SOFC cathode materials (Zhang *et al.*, 2008; Pang, Jiang, Li, Su *et al.*, 2012). The cationic ordering in $\text{LnBaCo}_2\text{O}_{6-\delta}$ layered perovskite oxides takes place because of the large difference

between the ionic radii of Ba^{2+} ($r_{\text{Ba}^{2+}} = 1.61 \text{ \AA}$) and Ln^{3+} ions ($r_{\text{Pr}^{3+}} = 1.179 \text{ \AA}$, $r_{\text{Nd}^{3+}} = 1.27 \text{ \AA}$, $r_{\text{Sm}^{3+}} = 1.24 \text{ \AA}$, $r_{\text{Gd}^{3+}} = 1.107 \text{ \AA}$). Fig. 1 shows an *A*-cationic disordered perovskite, where the La^{3+} and Ba^{2+} ions are randomly distributed (Fig. 1*a*), and an *A*-cationic ordered perovskite, where La^{3+} and Ba^{2+} are distributed in layers (Fig. 1*b*). The cubic and tetragonal unit cells are highlighted in these figures. As a consequence of the cationic ordering, the oxygen bond displays a different strength depending on whether it is located in BaO , CoO_2 or LnO layers, giving rise to differentiated oxygen crystallographic sites: O1, O2 and O3, respectively. Thus, for example, Taskin *et al.* (2005) reported that the cationic ordered $\text{GdBaMn}_2\text{O}_{6-\delta}$ perovskite exhibits a higher change of oxygen content and a higher rate of oxygen uptake than the cationic disordered $\text{Gd}_{0.5}\text{Ba}_{0.5}\text{MnO}_{3-x}$ perovskite. They assume that the cationic order in the crystal structure will reduce the oxygen bonding strength and will provide a disorder-free channel for ion motion. The reduction of oxygen bonding strength might also induce a two-dimensional distribution of oxygen vacancies in the (001) LnO layers (tetragonal symmetry, $P4mmm$) of layered cobaltites (Taskin *et al.*, 2005; Tarancón *et al.*, 2008; Streule, Podlesnyak, Sheptyakov *et al.*, 2006). In this way, linked $\text{Co}-\text{O}-\text{Co}$ channels subsist in CoO_2 layers even at high temperatures. Similarly to other perovskite-related oxides, the electronic conductivity in $\text{LnBaCo}_2\text{O}_{6-\delta}$ occurs *via* electron hopping along $\text{Co}-\text{O}-\text{Co}$ bonds with a double exchange process (Zhang *et al.*, 2008). Thus, the presence of linked $\text{Co}-\text{O}-\text{Co}$ channels permits high values of electrical conductivity to be achieved at high temperatures.

Despite this promoting characteristic of layered perovskites, recent work by Kim *et al.* (2009) shows that cationic disordered $\text{La}_{0.5}\text{Ba}_{0.5}\text{CoO}_{3-\delta}$ displays better ionic and electronic conductivities than cationic ordered $\text{LnBaCo}_2\text{O}_{6-\delta}$ ($\text{Ln} = \text{Pr}, \text{Nd}, \text{Sm}$), possibly because the former has a less distorted lattice. However, it is not clear if the improvement of transport properties is a consequence of cationic disorder or Ln nature.

Controlled syntheses of cationic ordered/disordered phases for the case $\text{Ln} = \text{La}$ ($r_{\text{La}^{3+}} = 1.36 \text{ \AA}$) (Nakajima *et al.*, 2005; Rautama *et al.*, 2009, 2008) have given the opportunity to study the effect of structure (independently of Ln nature) on high-temperature transport properties. Three characteristic

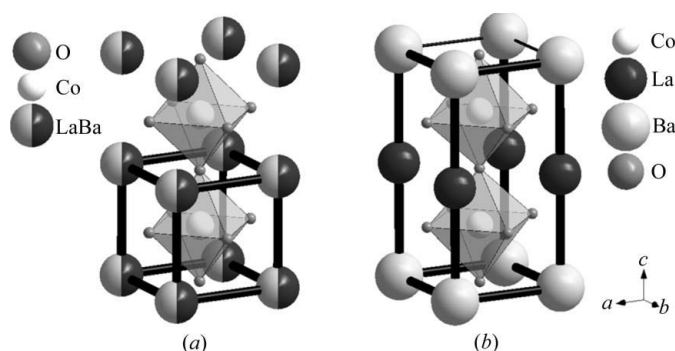


Figure 1
Schematic structures of (a) the cationic disordered $\text{La}_{0.5}\text{Ba}_{0.5}\text{CoO}_{3-\delta}$ phase and (b) the cationic ordered $\text{LaBaCo}_2\text{O}_{6-\delta}$ phase. The cubic and tetragonal unit cells are indicated.

structures were reported by Rautama *et al.* (2008) for this composition at room temperature: disordered cubic perovskite $\text{La}_{0.5}\text{Ba}_{0.5}\text{CoO}_3$, perfectly ordered layered $\text{LaBaCo}_2\text{O}_6$ and a nanoscale-ordered $\text{LaBaCo}_2\text{O}_6$. These structures were studied by neutron diffraction (Nakajima *et al.*, 2005), X-ray diffraction and electron diffraction (Rautama *et al.*, 2009, 2008) below room temperature. However, to the best of our knowledge, structural characterization of cationic disordered $\text{La}_{0.5}\text{Ba}_{0.5}\text{CoO}_3$ and cationic ordered $\text{LaBaCo}_2\text{O}_6$ structures at high temperatures has not been performed yet. Recently, S. Pang and co-workers have reported a comparative study of electrical conductivity at high temperature (Pang, Li *et al.*, 2012) and area-specific resistance (ASR) (Pang, Jiang, Li, Su *et al.*, 2012; Pang, Jiang, Li, Wang & Su, 2012) properties for $\text{La}_{0.5}\text{Ba}_{0.5}\text{CoO}_{3-\delta}$ and $\text{LaBaCo}_2\text{O}_{6-\delta}$. These authors found that, while the electrical conductivity for the cationic disordered $\text{La}_{0.5}\text{Ba}_{0.5}\text{CoO}_{3-\delta}$ phase is higher than that of ordered $\text{LaBaCo}_2\text{O}_{6-\delta}$, the ASR is lower. The ASR reaches values of $0.0086 \Omega \text{ cm}^{-2}$ for the ordered phase (Pang, Jiang, Li, Su *et al.*, 2012) and $0.013 \Omega \text{ cm}^{-2}$ for the disordered phase (Pang, Jiang, Li, Wang & Su, 2012) at 1073 K in air. These results suggest a strong influence of structural features on the electrochemical performance.

The electrochemical performance of cobaltites is influenced by O-ion and electron transport. The O-ion transport takes place with an O-vacancy mechanism involving hopping through the O sublattice, whereas the electron transport arises *via* electron holes in the $\text{Co}-\text{O}$ $3d-2p$ band. Neutron diffraction makes it possible to obtain information about the oxygen sublattice of crystalline oxides given its high sensitivity to oxygen in the presence of heavier rare earth and transition metal elements. This structural characterization, complemented with X-ray diffraction, gives useful information about oxygen and cation sublattices. Therefore, significant structural information could be obtained by combining the two techniques, and this structural information could be related to O-ion and electron-hole transport. Thus, for example, the effects of oxygen vacancies on structures and the determination of the O-diffusion path in perovskites and related structures such as $\text{Ba}_{0.5}\text{Sr}_{0.5}\text{Co}_{0.8}\text{Fe}_{0.2}\text{O}_{3-\delta}$ (McIntosh *et al.*, 2006; Itoh *et al.*, 2009, 2010), SrFeO_x (Schmidt & Campbell, 2002), $\text{NdBaCo}_2\text{O}_{5+x}$ (Hu *et al.*, 2012), $\text{PrBaCo}_2\text{O}_{5+\delta}$ (Chen *et al.*, 2013) and $\text{Sr}_3\text{Fe}(\text{Fe}, \text{Co}, \text{Ni})\text{O}_{6+\delta}$ (Mogni *et al.*, 2009) were studied from *in situ* neutron diffraction techniques.

In this work, we perform an *in situ* neutron powder diffraction study for cationic ordered $\text{LaBaCo}_2\text{O}_{6-\delta}$ and cationic disordered $\text{La}_{0.5}\text{Ba}_{0.5}\text{CoO}_{3-\delta}$ at room temperature and 673 K, in order to obtain detailed structural information that can be correlated with the intermediate-temperature properties of these oxides. The choice of 673 K as intermediate temperature is based on the fact that, at this temperature, the oxygen exchange and bulk diffusion in these materials are high enough to promote oxygen vacancy generation.

2. Experimental

Powder samples were obtained by the solid state reaction method (SSR). Stoichiometric amounts of La_2O_3 and Co_3O_4

oxides and BaCO_3 carbonate were mixed using an agate ball mill. The cationic ordered $\text{LaBaCo}_2\text{O}_{6-\delta}$ phase was obtained by annealing at 1423 K under Ar flow for 24 h, with heating and cooling rates of 2 K min^{-1} . Then, the powders were annealed at 673 K in air for 6 h in order to reach the equilibrium oxygen content. The cationic disordered $\text{La}_{0.5}\text{Ba}_{0.5}\text{CoO}_{3-\delta}$ phase was obtained by heat treating at 1373 K in air for 12 h, with heating and cooling rates of 5 K min^{-1} .

X-ray powder diffraction (XRD) patterns were collected at room temperature with a Philips PW1700 diffractometer using $\text{Cu K}\alpha$ radiation and a graphite monochromator. All reflection peaks of $\text{La}_{0.5}\text{Ba}_{0.5}\text{CoO}_{3-\delta}$ were indexed according to the cubic symmetry (space group $Pm\bar{3}m$) previously reported for this compound (Nakajima *et al.*, 2005), while those corresponding to $\text{LaBaCo}_2\text{O}_{6-\delta}$ were assigned to the tetragonal unit cell (space group $P4/mmm$) reported by the same authors.

Neutron powder diffraction (NPD) measurements were carried out at Institut Laue–Langevin (ILL), Grenoble, France, using the D2B powder diffractometer ($\lambda = 1.594 \text{ \AA}$). A vanadium sample holder was used for the measurements at room temperature and a quartz tube for the measurements at high temperature. The quartz tube was open, allowing oxygen exchange with the surrounding air. The high resolution of this two-axis diffractometer allowed a precise determination of the positions and occupation numbers of O atoms. All patterns were refined by the Rietveld method using the *FullProf* suite tools (Rodríguez-Carvajal, 2000). Details of the refinements are given in the supporting information.¹ The XRD and NPD room-temperature data were refined simultaneously in order to obtain complementary information. The Bond_Str (bond-valence parameters) and GFourier tools of *FullProf* were used for calculating the distances and angles in the crystal structures and for obtaining the Fourier maps, respectively.

The oxygen content of samples was determined *in situ* as a function of temperature in air by thermogravimetry (TG) using a symmetrical thermobalance based on a Cahn 1000 electrobalance. The mass change was associated with oxygen content by *a posteriori in situ* reduction under 10% H_2/Ar atmosphere. The final products of reduction, La_2O_3 , BaO and Co , were checked by XRD. This oxygen content determination was used as an independent measure of total oxygen vacancies. The oxygen content for the cationic disordered phase was also determined under an oxygen partial pressure $p\text{O}_2 = 2 \times 10^{-3} \text{ atm}$ ($1 \text{ atm} = 101\,325 \text{ Pa}$), making use of an electrochemical system of an oxygen pump and a sensor in Ar as gas carrier.

Dense samples were obtained by pressing $\text{La}_{0.5}\text{Ba}_{0.5}\text{CoO}_{3-\delta}$ and $\text{LaBaCo}_2\text{O}_{6-\delta}$ powders followed by a heat treatment at 1373 K for 6 h in air and 1423 K for 6 h in Ar, respectively. Resistivity measurements on these dense samples were performed by the four-probe technique. Resistivity (ρ) curves as a function of temperature (T) were collected in air for temperatures ranging between 273 and 1173 K. Conductivity data were obtained from the relation $\sigma = \rho^{-1}$.

3. Results and discussion

3.1. Structural analysis

The diffraction pattern profile depends on structural parameters (symmetry, lattice parameters, atom positions, occupancies and vibration, *etc.*) and microstructural parameters (grain size and microstrain effect). The structural models used for $\text{La}_{0.5}\text{Ba}_{0.5}\text{CoO}_{3-\delta}$ and $\text{LaBaCo}_2\text{O}_{6-\delta}$ are based on those of cubic $\text{La}_{0.5}\text{Sr}_{0.5}\text{CoO}_{3-\delta}$ (Setevich *et al.*, 2012) and tetragonal $\text{PrBaCo}_2\text{O}_{6-\delta}$ (Nakajima *et al.*, 2005; Frontera *et al.*, 2005), respectively. The models tested to refine the crystal structures are discussed in the supplementary information. These models included microstrain effects, considerations about isotropic or anisotropic atomic relative vibrational motion, and the location and values of oxygen vacancy defects.

The goodness of fits for the samples were improved by considering the phenomenological Stephens model (Stephens, 1999) for the anisotropic microstrain effect and including anisotropic and isotropic Debye–Waller coefficients for thermal atomic vibration for $\text{LaBaCo}_2\text{O}_{6-\delta}$ and $\text{La}_{0.5}\text{Ba}_{0.5}\text{CoO}_{3-\delta}$. Besides, in both compounds, the O content was fixed to equal the values obtained from independent TG measurement to avoid any correlation between the O occupation and thermal displacement.

Fig. 2 shows the normalized O content obtained from TG as a function of T for $\text{LaBaCo}_2\text{O}_{6-\delta}$ and $\text{La}_{0.5}\text{Ba}_{0.5}\text{CoO}_{3-\delta}$. The data at room temperature and 673 K are used to fit the NPD profile, obtaining the best agreement at 673 K. Figs. 3 and 4 show the NPD measured and calculated profiles, and the difference between the two, for $\text{La}_{0.5}\text{Ba}_{0.5}\text{CoO}_{3-\delta}$ and for $\text{LaBaCo}_2\text{O}_{6-\delta}$, respectively. The structural data obtained from these refinements are discussed below.

Tables 1 and 2 show the structural and microstructural parameters determined from Rietveld analysis for $\text{La}_{0.5}\text{Ba}_{0.5}\text{CoO}_{3-\delta}$ and $\text{LaBaCo}_2\text{O}_{6-\delta}$, respectively. Structural features such as lattice parameters (a , b and c), specific atomic positions (x , y , z) and occupancies (g_{atom}), and the equivalent thermal displacements (B_{iso}), are shown for both samples at

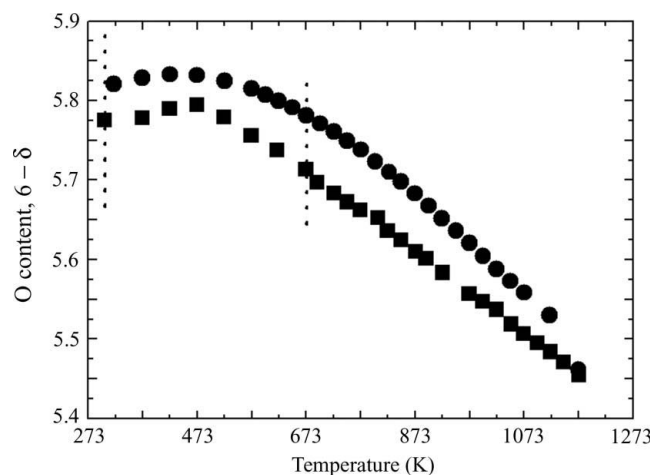


Figure 2

Oxygen content of samples as a function of T , obtained by *in situ* thermogravimetric measurement. Black squares: $(6 - \delta)$, $\text{LaBaCo}_2\text{O}_{6-\delta}$; black circles: $2 \times (3 - \delta)$, $\text{La}_{0.5}\text{Ba}_{0.5}\text{CoO}_{3-\delta}$.

¹ Supporting information for this article is available from the IUCr electronic archives (Reference: FS5049).

Table 1

Structural parameters of $\text{La}_{0.5}\text{Ba}_{0.5}\text{CoO}_{3-\delta}$ at room temperature and 673 K.

The space group is cubic $Pm\bar{3}m$.

Atom	Room temperature		673 K	
	g_{atom}	$B_{\text{iso}} (\text{\AA}^2)$	g_{atom}	$B_{\text{iso}} (\text{\AA}^2)$
Co (1/2, 1/2, 1/2)	1	0.25 (5)	1	0.95 (5)
Ba (0, 0, 0)	0.5	0.43 (3)	0.5	1.01 (5)
La (0, 0, 0)	0.5	0.43 (3)	0.5	1.01 (5)
O (1/2, 1/2, 0)	0.97 (1)	1.39 (4)	0.96 (1)	1.98 (3)
Lattice parameters (Å)	$a = b = c = 3.89151 (5)$		$a = b = c = 3.91979 (4)$	
O content	$3 - \delta = 2.91$		$3 - \delta = 2.88$	
$V_{\text{uc}} (\text{\AA}^3)$	58.932 (3)		60.227 (2)	
$\rho (\text{Mg m}^{-3})$	6.8627 (3)		6.7065 (2)	
Max-strain (%)†	35.4 (1)		33.1 (4)	

† The symbol (%) indicates that the unit is divided by 10 000.

room temperature and 673 K. Values of anisotropic atomic displacement parameters and information about the refinements are included in the supplementary data. In both samples, as the temperature increases, the O occupancies (g_{O}) decrease, while the mean atomic displacements increase. The two parameters might be strongly correlated, in which case,

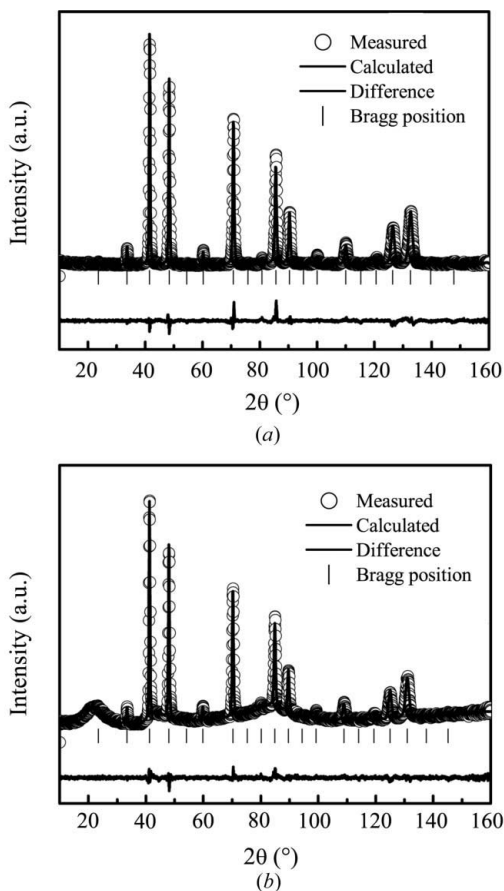


Figure 3

NPD profile fitting at (a) room temperature ($\chi^2 = 4.49$, $R_p = 16.1$ and $R_{\text{wp}} = 13.7$) and (b) 673 K ($\chi^2 = 1.73$, $R_p = 19.9$ and $R_{\text{wp}} = 11.6$) for $\text{La}_{0.5}\text{Ba}_{0.5}\text{CoO}_{3-\delta}$ with anisotropic strain, isotropic vibration and O content fixed.

Table 2

Structural parameters of $\text{LaBaCo}_2\text{O}_{6-\delta}$ at room temperature and 673 K.

The space group is cubic $P4mmm$.

Atom	Room temperature			673 K		
	z	g_{atom}	$B_{\text{iso}} (\text{\AA}^2)$	z	a_{atom}	$B_{\text{iso}} (\text{\AA}^2)$
Co (1/2, 1/2, z)	0.2490 (9)	1	0.17	0.2486 (1)	1	0.97
Ba (0, 0, 0)	–	1	0.06	–	1	0.52
La (0, 0, 1/2)	–	1	0.39	–	1	1.43
O1 (1/2, 1/2, 0)	–	1	0.75	–	1	1.60
O2 (1/2, 0, z)	0.2694 (3)	1	0.89	0.2693 (3)	1	1.75
O3 (1/2, 1/2, 1/2)	–	0.77 (1)	0.13	–	0.71 (1)	0.56
Lattice parameters (Å)	$a = b = 3.91468 (3)$, $c = 7.69992 (8)$			$a = b = 3.93654 (4)$, $c = 7.76284 (9)$		
O content	$6 - \delta = 5.77$			$6 - \delta = 5.71$		
$V_{\text{uc}} (\text{\AA}^3)$	117.999 (3)			120.295 (4)		
$\rho (\text{Mg m}^{-3})$	6.8446 (3)			6.7004 (4)		
Max-strain (%)†	20 (5)			18 (5)		

† The symbol (%) indicates that the unit is divided by 10 000.

fixing the oxygen content with an independent technique would allow a better resolution of B_{iso} . For the cationic ordered phase, three different oxygen positions can be distinguished, O1, O2 and O3, located in BaO, CoO_2 and LaO

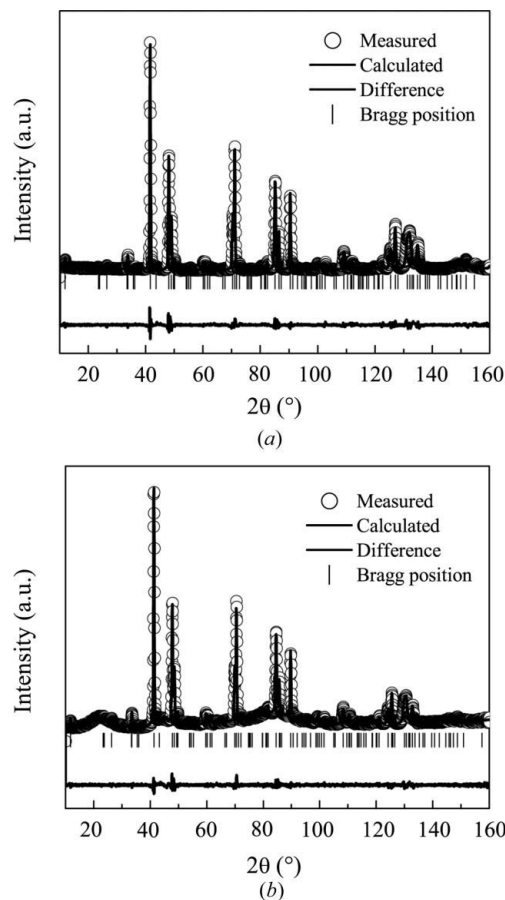


Figure 4

NPD profile fitting at (a) room temperature ($\chi^2 = 5.09$, $R_p = 15.7$ and $R_{\text{wp}} = 13.3$) and (b) 673 K ($\chi^2 = 2.80$, $R_p = 17.2$ and $R_{\text{wp}} = 12.0$) for $\text{LaBaCo}_2\text{O}_{6-\delta}$ with anisotropic strain and vibration and O content fixed.

layers, respectively. Initially, the O vacancies were fully located on O3 sites. The B_{iso} values of the O1 and O2 sites were larger than that of the O3 site, suggesting that these O-atom sites could collaborate with the oxygen migration diffusion path. Considering this, the occupancies g_{O1} and g_{O2} were also released to be adjusted, and it was found that only the O2 and O3 sites can accept O vacancies. Therefore, it is possible to assume that, similar to the isostructural $\text{LnBaCo}_2\text{O}_6$ (Ln = Pr, Nd, Sm, Gd) compounds, the oxygen vacancies are mainly located in LaO layers (Streule, Podlesnyak, Pomjakushina *et al.*, 2006), while the O atoms located in CoO_2 layers facilitate the oxygen diffusion process. Recent studies of the diffusional pathway of O^{2-} ions in $\text{PrBaCo}_2\text{O}_{6-\delta}$ (Chen *et al.*, 2013) and $\text{NdBaCo}_2\text{O}_{6-\delta}$ layered perovskites (Hu *et al.*, 2012) by *in situ* neutron diffraction at temperatures higher than 873 K are consistent with our results.

Comparing the O content of cationic ordered and disordered phases in Fig. 2 and Tables 1 and 2, one can observe that the concentration of oxygen vacancies is higher for the $\text{LaBaCo}_2\text{O}_{6-\delta}$ ordered phase than for the $\text{La}_{0.5}\text{Ba}_{0.5}\text{CoO}_{3-\delta}$ phase over the whole temperature range. However, the O-atom displacement in the cationic disordered phase is larger than that in the ordered one, suggesting a higher delocalization or mobilization degree for O in the $\text{La}_{0.5}\text{Ba}_{0.5}\text{CoO}_{3-\delta}$ structure.

From the point of view of microstructural features, it was possible to obtain information about size and microstrain effects on peak profile by using a calibration function. While the size of domain seems to have a negligible effect on the broadening, the microstrain effect is evident in both structures. The maximum strains (Max-strain) are the average values calculated using the reciprocal lattice directions. In this way, the symmetry of each phase is taken into account and the standard deviations of Max-strain are a measure of the degree of anisotropy. Therefore, despite the fact that $\text{LaBaCo}_2\text{O}_{6-\delta}$ shows less stress than $\text{La}_{0.5}\text{Ba}_{0.5}\text{CoO}_{3-\delta}$, the cationic order

renders a more anisotropic strain. Fig. 5 shows the Williamson–Hall plots of integral breadth as a function of reciprocal distance for $\text{LaBaCo}_2\text{O}_{6-\delta}$ and $\text{La}_{0.5}\text{Ba}_{0.5}\text{CoO}_{3-\delta}$ samples at 673 K. The relative strain of the two samples and its anisotropic characteristic can be observed in these plots. These results are similar to those obtained at room temperature. The lower degree of anisotropy for the cationic disordered phase compared to ordered $\text{LaBaCo}_2\text{O}_{6-\delta}$ might be related to the cubic symmetry of this phase. In the cationic ordered phase, the more strained reflections are those corresponding to Miller indices $h00$, $0k0$ and $hk0$. The preferential strain direction suggests that some kind of local cationic disorder should be present in these directions despite the global ordering along the c axis. Besides, additional strain effects associated with some degree of ordering in the O sublattice should not be discarded. The O vacancies located in LaO layers could be ordered in chains along the **a** or **b** direction like in other isostructural $\text{LnBaCo}_2\text{O}_6$ (Ln = Pr, Nd, Sm, Gd) perovskites (Streule, Podlesnyak, Pomjakushina *et al.*, 2006). In the $\text{LnBaCo}_2\text{O}_6$ (Ln = Pr, Nd, Sm, Gd) compounds, the O-vacancy order is responsible for the existence of a low-temperature orthorhombic phase. Likewise, but with a minor degree of anisotropy, the highest strain is present along the $(h00)$ plane and the equivalent $(0k0)$ and $(00l)$ planes in the cubic phase. The high strain present in the $\text{La}_{0.5}\text{Ba}_{0.5}\text{CoO}_{3-\delta}$ sample might suggest that the cationic ordered $\text{LaBaCo}_2\text{O}_{6-\delta}$ phase is structurally more favorable.

3.2. Oxygen vacancy structure and O-migration path

Fig. 2 shows that the concentration of oxygen vacancies is higher in the cationic ordered $\text{LaBaCo}_2\text{O}_{6-\delta}$ phase than in cationic disordered $\text{La}_{0.5}\text{Ba}_{0.5}\text{CoO}_{3-\delta}$ in the whole temperature range. Therefore, we might assume that oxygen is more strongly bonded to the lattice in $\text{La}_{0.5}\text{Ba}_{0.5}\text{CoO}_{3-\delta}$ than in $\text{LaBaCo}_2\text{O}_{6-\delta}$. Besides, as has been observed from the structural analysis in the previous section, the oxygen vacancies of $\text{LaBaCo}_2\text{O}_{6-\delta}$ are preferentially located in O3 sites along LaO layers. These behaviors might be explained in the frame of the bond valence formalism.

Table 3 shows the bond valence sum (BVS) and some characteristic distances between atoms for both structures at room temperature and 673 K. The BVS of the oxygen sites follows the sequence $\text{O3}_{P4/mmm} < \text{O2}_{P4/mmm} \simeq \text{O}_{Pm\bar{3}m} < \text{O1}_{P4/mmm}$. In addition, these values decrease as temperature increases for both samples. Lower BVS values indicate that O is weakly bonded to the lattice (Chen *et al.*, 2013). Therefore, this result is in agreement with the fact that cationic order induces a highly defective structure with oxygen vacancies distributed along LaO layers.

In addition, the atomic displacements become anisotropic as a consequence of cationic order. Fig. 6 shows the atomic displacement (75% probability surface) at 673 K for both phases. Two unit cells of $\text{La}_{0.5}\text{Ba}_{0.5}\text{CoO}_{3-\delta}$ were included for comparison with $\text{LaBaCo}_2\text{O}_{6-\delta}$. The anisotropic atomic displacement in layered $\text{LaBaCo}_2\text{O}_{6-\delta}$ suggests that the O1 sites ($U_{11} = U_{22} > U_{33}$) move parallel to the BaO plane,

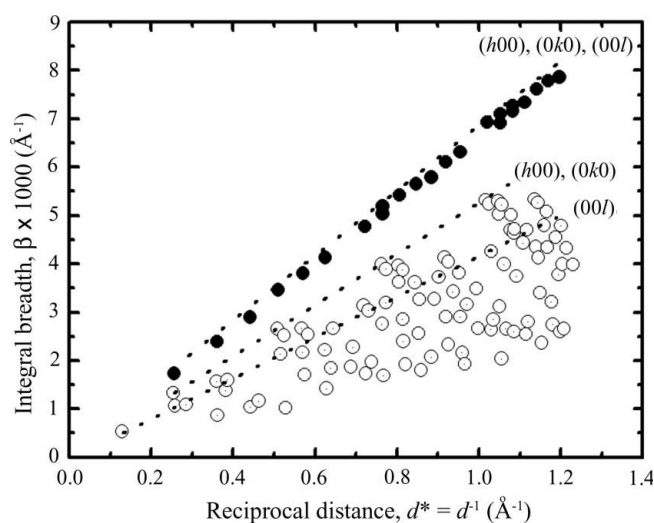


Figure 5
Williamson–Hall plot of integral breadths as a function of reciprocal distances obtained from Rietveld analysis at 673 K for $\text{LaBaCo}_2\text{O}_{6-\delta}$ (open circles) and $\text{La}_{0.5}\text{Ba}_{0.5}\text{CoO}_{3-\delta}$ (filled circles) samples.

Table 3

Bond valence sums (BVSs) and characteristic atomic distances (d) and angles obtained at room temperature and 673 K for $\text{La}_{0.5}\text{Ba}_{0.5}\text{CoO}_{3-\delta}$ and $\text{LaBaCo}_2\text{O}_{6-\delta}$.

$\text{La}_{0.5}\text{Ba}_{0.5}\text{CoO}_{3-\delta}$.

	BVS			d (Å), angles (°)	
	293 K	673 K		293 K	673 K
Co	3.161 (1)	3.022 (1)	Co—O ($\times 6$)	1.94575 (2)	1.95989 (2)
			O—Co—O	180.000 (3)	180.000 (2)
O	2.070 (1)	1.978 (1)	O—O ($\times 8$)	2.75171 (2)	2.771710 (20)

$\text{LaBaCo}_2\text{O}_{6-\delta}$.

	BVS			d (Å), angles (°)	
	293 K	673 K		293 K	673 K
Co	3.09 (1)	2.96 (1)	Co—O1 ($\times 2$)	1.914 (6)	1.930 (7)
			Co—O2 ($\times 4$)	1.9642 (5)	1.9748 (6)
			Co—O3 ($\times 2$)	1.936 (6)	1.952 (7)
			O2—Co—O2	170.42 (2)	170.67 (2)
O1	2.26 (1)	2.17 (2)	O1—O2 ($\times 8$)	2.855 (2)	2.871 (2)
O2	2.028 (2)	1.948 (2)	O2—O1 ($\times 2$)	2.855 (2)	2.871 (2)
			O2—O2 ($\times 4$)	2.76810 (2)	2.78355 (2)
			O2—O3 ($\times 2$)	2.640 (2)	2.661 (2)
O3	1.92 (1)	1.84 (1)	O3—O2 ($\times 8$)	2.6401 (16)	2.661 (2)
			O3—O3 ($\times 4$)	3.91468 (3)	3.93654 (4)

whereas the O2 sites ($U_{33} > U_{11} \times U_{22}$) distort the CoO_6 octahedra, moving along the c axis toward the O3 sites, which exhibit a shorter and almost isotropic atomic displacement. The O-atom displacement in the $\text{La}_{0.5}\text{Ba}_{0.5}\text{CoO}_{3-\delta}$ structure is larger than those of $\text{LaBaCo}_2\text{O}_{6-\delta}$. Therefore, we might assume that the O atoms in $\text{La}_{0.5}\text{Ba}_{0.5}\text{CoO}_{3-\delta}$ are more mobile than O2 and O3 in $\text{LaBaCo}_2\text{O}_{6-\delta}$, because although they are more strongly bonded to the lattice (high BVS) their mean displacements are larger. The possible O-migration pathways are indicated by arrows in Fig. 6. The O-migration paths were proposed considering the anisotropic or isotropic atomic displacement and the Fourier maps shown in Fig. 7. The Fourier maps were obtained from the structure factors observed (NPD-Fobs) and the phase calculated from Rietveld analysis of NPD data using GFourier tools. Fig. 7(a) shows the Fourier maps of the (200) Co—O plane in cubic perovskite at 673 K. The (200) plane is equivalent to the (020) and (002) planes because of the cubic symmetry. Figs. 7(b) and 7(c) show the Fourier maps of the (004) and (200) [or (020)] Co—O planes, respectively. As observed, while all the Co—O planes in $\text{La}_{0.5}\text{Ba}_{0.5}\text{CoO}_{3-\delta}$ and that normal to the c direction in $\text{LaBaCo}_2\text{O}_{6-\delta}$ exhibit an isotropically distributed neutron density, the neutron densities of Fourier maps parallel to the c direction are concentrated toward LaO planes. The Fourier maps and the O-atom displacements suggest a two-dimensional character

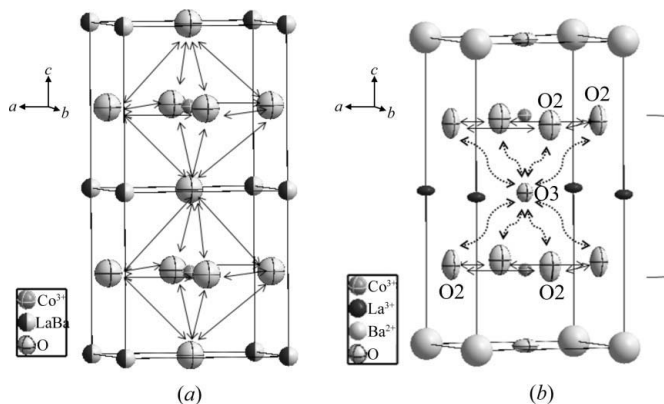


Figure 6

Crystal structure obtained from refinement at 673 K of (a) $\text{La}_{0.5}\text{Ba}_{0.5}\text{CoO}_{3-\delta}$ and (b) $\text{LaBaCo}_2\text{O}_{6-\delta}$. Atoms are represented as ellipsoids of 75% probability. Arrows are guide to the eyes indicating possible O-migration path.

for the O-migration path in $\text{LaBaCo}_2\text{O}_{6-\delta}$ in contrast to the three dimensions in $\text{La}_{0.5}\text{Ba}_{0.5}\text{CoO}_{3-\delta}$. Besides, considering the O—O distances in Table 3, it might be expected that the O migration for $\text{LaBaCo}_2\text{O}_{6-\delta}$ structures involves mainly O2—O3 and O2—O2 hopping because these distances are shorter than the O3—O3 distances.

Kim *et al.* (2009) compared the ionic and electronic conductivity of disordered $\text{La}_{0.5}\text{Ba}_{0.5}\text{CoO}_{3-\delta}$ with those of cationic ordered $\text{LnBaCo}_2\text{O}_{6-\delta}$ ($\text{Ln} = \text{Pr}, \text{Nd}, \text{Sm}$). They found that O-permeation flow in these materials is bulk limited by O-ion diffusion and that the cubic perovskite $\text{La}_{0.5}\text{Ba}_{0.5}\text{CoO}_{3-\delta}$ has the higher ionic (σ_{ion}) and electronic (σ_{el}) conductivity. On the other hand, Zhang *et al.* (2008) compared these properties for the layered perovskite series $\text{LnBaCo}_2\text{O}_{6-\delta}$ ($\text{Ln} = \text{La}, \text{Pr}, \text{Nd}, \text{Sm}, \text{Gd}, \text{Y}$). Despite the difference between absolute values of ionic conductivity reported in the two works, σ_{ion} follows the series $\text{La}_{0.5}\text{Ba}_{0.5}\text{CoO}_{3-\delta} > \text{PrBaCo}_2\text{O}_{6-\delta} > \text{NdBaCo}_2\text{O}_{6-\delta} \gg \text{SmBaCo}_2\text{O}_{6-\delta} > \text{GdBaCo}_2\text{O}_{6-\delta} > \text{LaBa}$

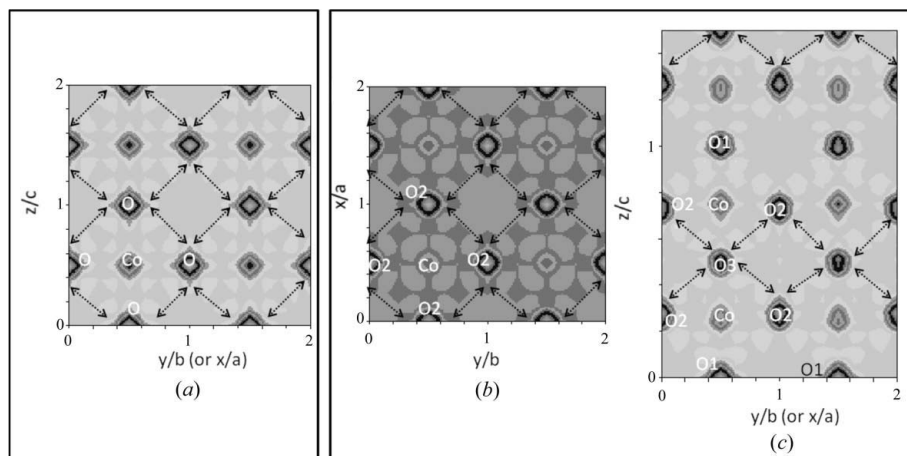


Figure 7

Fourier maps of neutron density obtained at 673 K from NPD data. CoO layers corresponding to (a) the (200) plane for $\text{La}_{0.5}\text{Ba}_{0.5}\text{CoO}_{3-\delta}$, and (b) the (004) plane and (c) the (200) plane for $\text{La}_{0.5}\text{Ba}_{0.5}\text{CoO}_{3-\delta}$.

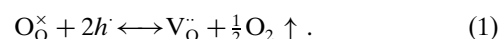
$\text{Co}_2\text{O}_{6-\delta}$. Therefore, the diffusion mechanism proposed in this work, involving a three-dimensional pathway for $\text{La}_{0.5}\text{Ba}_{0.5}\text{CoO}_{3-\delta}$ and a two-dimensional one for $\text{LaBaCo}_2\text{O}_{6-\delta}$, would explain the higher ionic conductivity for the cationic disordered phase in spite of their lower O-vacancy concentration.

3.3. Electrical conductivity and electron-hole transport

The equilibrium electrical conductivities (σ) of $\text{LaBaCo}_2\text{O}_{6-\delta}$ and $\text{La}_{0.5}\text{Ba}_{0.5}\text{CoO}_{3-\delta}$ dense samples have been measured as a function of temperature between 293 and 1173 K in air. Usually in these cobalt-rich perovskites, the ionic conductivity ranges from 10^{-2} to 10^{-1} S cm^{-1} and the electronic conductivity is between 100 and 1000 S cm^{-1} (Zhang *et al.*, 2008; Kim *et al.*, 2009); therefore it is a good approximation to consider that the electron conductivity almost equals the total electrical conductivity. Fig. 8(a) shows the σ versus T curves. As observed, the conductivity remains almost constant with T below 523 K for both samples. On increasing T above 523 K, the conductivities decrease, exhibiting a metallic like behavior. Besides, the electrical conductivity of $\text{LaBaCo}_2\text{O}_{6-\delta}$ is lower than that of

$\text{La}_{0.5}\text{Ba}_{0.5}\text{CoO}_{3-\delta}$, but both are higher than those reported for other perovskites, which achieve maximum conductivity values around 200–500 S cm^{-1} at 673 K (Tai *et al.*, 1995; Zhang *et al.*, 2008; Suntssov *et al.*, 2011). The fact that the electrical conductivity of $\text{LaBaCo}_2\text{O}_{6-\delta}$ is lower than that of $\text{La}_{0.5}\text{Ba}_{0.5}\text{CoO}_{3-\delta}$ is in agreement with the previous results reported by Pang, Li *et al.* (2012).

Comparing Figs. 2 and 8(a), it is possible to correlate the behavior of σ with T to the change of oxygen content. In such a case, the conductivity would be p-type, with electron-hole (h') charge carriers (Pang, Li *et al.*, 2012) hopping from Co^{4+} to Co^{3+} ions through the Co 3d–O 2p band (Zhang *et al.*, 2008). Therefore, using the Kroger–Vink notation, oxygen vacancies V_{O}^{\bullet} are created as T increases, consuming the electron holes according to



Combining electrical conductivity data with oxygen content data as a function of T , the dependence of σ versus ‘normalized’ oxygen content ($6-\delta$) is plotted in Fig. 8(b), showing that, effectively, for both samples the conductivity increases with $6-\delta$.

One can notice from Fig. 2 that the oxygen content in $\text{La}_{0.5}\text{Ba}_{0.5}\text{CoO}_{3-\delta}$ is higher than that of $\text{LaBaCo}_2\text{O}_{6-\delta}$ at the same temperature, rendering higher conductivity values (see Fig. 8). However, one additional factor influencing the conductivity behavior seems to be present. With the aim of discriminating some structural effect on conductivity, in addition to the O-vacancy effect, a different *in situ* condition was selected for the cationic disordered phase. The oxygen content for this sample was determined using the thermobalance coupled to a gas blending system. This system allowed the determination of the oxygen content at $p\text{O}_2 = 0.002$ atm between room temperature and 1173 K. From these experiments we were able to determine that, at 673 K and $p\text{O}_2 = 0.002$ atm, the unit formula of the cationic disordered phase is $\text{La}_{0.5}\text{Ba}_{0.5}\text{CoO}_{2.36}$. This $3-\delta$ value corresponds to the same normalized oxygen content as for the cationic ordered phase $\text{LaBaCo}_2\text{O}_{5.72}$ at 673 K in air. Then, fixing $p\text{O}_2$ at 0.002 atm the equilibrium electrical conductivity was measured at 673 K. This unique point is also included in Figs. 8(a) and 8(b) (marked as open triangles). It was found that the electronic conductivity in the cationic disordered phase ($\text{La}_{0.5}\text{Ba}_{0.5}\text{CoO}_{3-\delta}$) is higher than that in cationic ordered $\text{LaBaCo}_2\text{O}_{6-\delta}$, regardless of the oxygen vacancy concentration, the structural properties being key to controlling the electron transport.

The metallic like behavior and the decrease of conductivity as the concentration of oxygen vacancies decreases (at constant temperature) suggest the presence of an electron-hole mechanism controlling the electrical transport. Most cobaltites with perovskite structure show a small polaron mobility controlling the electron-hole mechanism (Tai *et al.*, 1995; Zhang *et al.*, 2008; Sehlín *et al.*, 1995). In these cases, the electron holes move slowly along the polar oxides, dragging a polarization cloud. Then, a thermally activated dependence is observed for conductivity data:

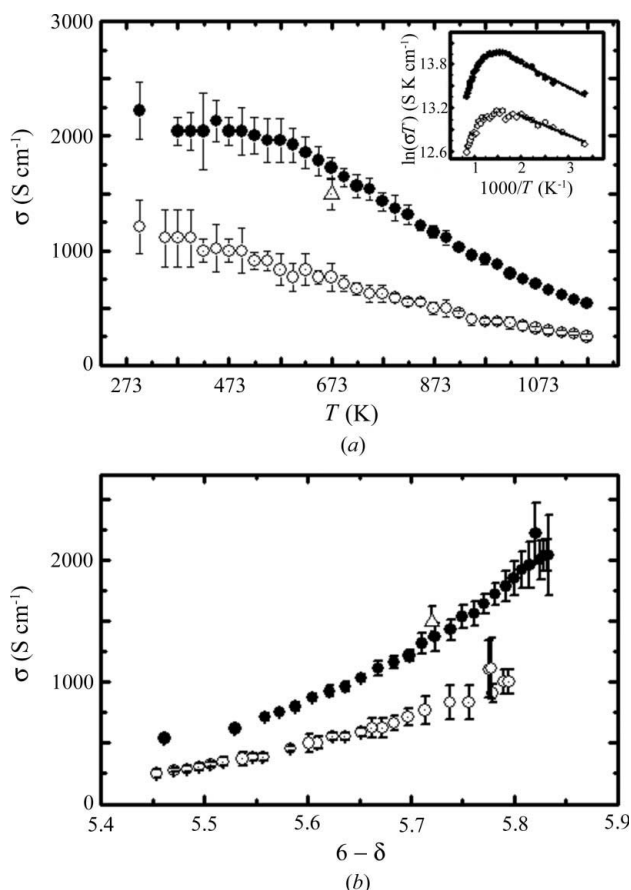


Figure 8 $\text{LaBaCo}_2\text{O}_{6-\delta}$ and $\text{La}_{0.5}\text{Ba}_{0.5}\text{CoO}_{3-\delta}$ equilibrium electrical conductivities (σ) as a function of (a) temperature, T , and (b) normalized oxygen content of samples, $6-\delta$, in air. The Arrhenius plot, $\ln(\sigma T)$ versus T^{-1} , is shown in the inset. Open circles: $\text{LaBaCo}_2\text{O}_{6-\delta}$; filled circles: $\text{La}_{0.5}\text{Ba}_{0.5}\text{CoO}_{3-\delta}$; open triangles: $\text{La}_{0.5}\text{Ba}_{0.5}\text{CoO}_{2.36}$.

Table 4

Electron-hole mobility (μ) and lineal mobility (μ_{lineal}) of $\text{La}_{0.5}\text{Ba}_{0.5}\text{CoO}_{3-\delta}$ and $\text{LaBaCo}_2\text{O}_{6-\delta}$ at room temperature and 673 K.

Sample	Temperature (K)	μ ($\text{cm}^2 \text{V}^{-1} \text{s}^{-1}$)	μ_{lineal} ($\text{cm}^2 \text{V}^{-1} \text{s}^{-1}$)
$\text{LaBaCo}_2\text{O}_{6-\delta}$	293	1.48	0.37
	673	1.35	0.34
$\text{La}_{0.5}\text{Ba}_{0.5}\text{CoO}_{3-\delta}$	293	2.49	0.41
	673	2.22	0.37

$$\sigma = |e|\mu p = |e|p \frac{\mu_0}{T} \exp\left(\frac{-E_a}{k_B T}\right), \quad (2)$$

where e is the electron charge, μ is the electron-hole mobility, p is the electron-hole concentration per unit-cell volume, E_a is the activation energy and k_B is the Boltzmann constant. Under constant electron-hole concentration, if the activation energy is low, the exponential pre-factor depending on T would dominate, causing the conductivity to decrease as T increases.

The inset in Fig. 8(a) shows both Arrhenius plots [$\ln(\sigma T)$ versus T^{-1}]. The E_a values of $\text{LaBaCo}_2\text{O}_{6-\delta}$ and $\text{La}_{0.5}\text{Ba}_{0.5}\text{CoO}_{3-\delta}$ were computed between room temperature and 523 K, where the oxygen content and the electron-hole concentration remain almost constant. The activation energies obtained, $E_a^{\text{LaBaCo}_2\text{O}_{6-\delta}} = 0.019$ eV and $E_a^{\text{La}_{0.5}\text{Ba}_{0.5}\text{CoO}_{3-\delta}} = 0.030$ eV, are almost negligible, suggesting that these are not thermally activated processes. Therefore, the electron-hole transport should correspond to a large polaron.

The main difference between small and large polarons is their mobility values. In the first case the interaction between electron hole and lattice is strong, rendering the highest localization of charge. The electron holes, occupying a narrow band, hop between Co^{4+} and Co^{3+} sites. The characteristic mobility values for small polarons are between 10^{-4} and $10^{-5} \text{cm}^2 \text{V}^{-1} \text{s}^{-1}$. In the case of the large-polaron mechanism, the charge carriers are itinerant, moving almost freely along a wide band. The behavior is metallic like, but the mobility ($1\text{--}10 \text{cm}^2 \text{V}^{-1} \text{s}^{-1}$) is still lower than that of metallic conductors. Therefore, from the mobility for both phases computed using equation (2) and conductivity data, the electron transport mechanism could be proposed.

In both La–Ba–Co–O systems studied in this work, the negative charges Ba'_{La} produced when La^{3+} ions are partially replaced by Ba^{2+} ions must be compensated for by electron-hole creation at the Co sites (h') and oxygen vacancy generation at O sites ($V_{\text{O}}^{\cdot\cdot}$). The charge balance is

$$2[V_{\text{O}}^{\cdot\cdot}] + [h'] = [\text{Ba}'_{\text{La}}]. \quad (3)$$

The electron-hole concentration $p = h' / V_{\text{uc}}$ (V_{uc} is the unit-cell volume) can be estimated considering $V_{\text{O}}^{\cdot\cdot} = \delta$ and Ba'_{La} equal to 1 and 0.5 for $\text{LaBaCo}_2\text{O}_{6-\delta}$ and $\text{La}_{0.5}\text{Ba}_{0.5}\text{CoO}_{3-\delta}$, respectively. Therefore, the mobility values are obtained from equation (2) using the electron-hole concentration estimated from oxygen content. In the third column of Table 4 the electron-hole mobility values estimated at 293 and 673 K are listed. On one hand, in both samples the mobility decreases with T . This behavior and the mobility values themselves are typical of large-polaron behavior. On the other hand, the

electron-hole mobility in the cationic disordered phase is almost twice that of the cationic ordered phase at both temperatures. Analyzing the Co–O distances and angles given in Table 3, the differences between them are not sufficient to explain the difference between mobility values.

If the two-dimensional character of layered perovskites as opposed to the three-dimensional structure of cubic perovskites is considered, it might be probable that, instead of six equivalent directions to electron-hole movements, in layered perovskites there are only four. The electronic density of these compounds was studied from the XRD Fourier maps. The results of this study are shown in Fig. 9. Figs. 9(a) and 9(b) show the Co–O layers corresponding to the (002) and (200) planes of $\text{La}_{0.5}\text{Ba}_{0.5}\text{CoO}_{3-\delta}$, respectively, whereas Figs. 9(c) and 9(d) show the Co–O2 and Co–O (O1, O2 and O3) layers corresponding to the (004) and (200) planes of $\text{LaBaCo}_2\text{O}_{6-\delta}$, respectively. The electronic density is more isotropically distributed in the cationic disordered phase than in the cationic ordered one, where the c direction shows a lack of electronic density around the O3 site. Therefore, it is plausible to assume that the oxygen vacancies, preferentially located in the LaO layer, work as a barrier blocking the charge carrier movement through the Co $3d$ –O $2p$ band in the c -axis direction. This way, it is possible to define a lineal mobility such as $\mu_{\text{lineal}}^{\text{La}_{0.5}\text{Ba}_{0.5}\text{CoO}_{3-\delta}} = \mu/6$ for the cubic symmetry and $\mu_{\text{lineal}}^{\text{LaBaCo}_2\text{O}_{6-\delta}} = \mu/4$ for the tetragonal one. The lineal mobility values are also shown in Table 4.

The lineal mobility of the cationic ordered phase is slightly lower than that of the cationic disordered phase. The differences between electron-hole mobility arise from the octahedral distortion produced by La–Ba cationic order. As

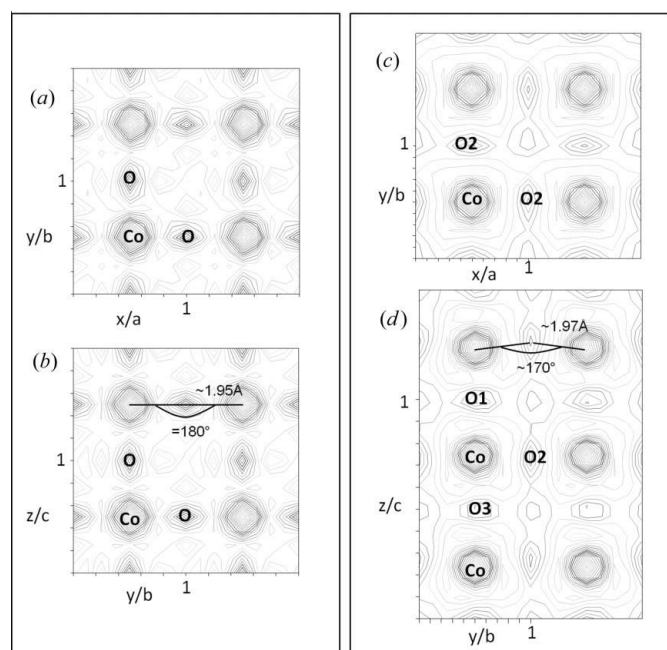


Figure 9 Fourier maps of electron density obtained at room temperature from XRD data. Co–O layers corresponding to (a) the (002) plane and (b) the (200) plane for $\text{La}_{0.5}\text{Ba}_{0.5}\text{CoO}_{3-\delta}$, and (c) the (004) plane and (d) the (200) plane for $\text{LaBaCo}_2\text{O}_{6-\delta}$.

observed in Table 3 and Fig. 9, in cationic ordered phases the O—Co—O angles are lower than 180° , locating these atoms out of the *ab* plane. This fact, as well as the increment in the Co—O distances (see Table 3), reduces the overlapping between the Co 3*d* and O 2*p* orbitals in LaBaCo₂O_{6- δ} compared to La_{0.5}Ba_{0.5}CoO_{3- δ} , decreasing the electron-hole mobility.

Therefore, although these cobaltites are better electronic conductors than other perovskites, the structural difference between them improves the electronic conduction in La_{0.5}Ba_{0.5}CoO_{3- δ} compared to LaBaCo₂O_{6- δ} . This would be due to the fact that, in LaBaCo₂O_{6- δ} , the conductivity is two dimensional instead of three dimensional. Besides, the loss of overlapping between the Co 3*d* and O 2*p* orbitals due to the octahedral distortion hampers the electron-hole transport.

4. Conclusions

The effect of cationic ordering or disordering on ionic and electronic transport properties of cobalt perovskites was analyzed in relation to the structural features determined by NPD and XRD techniques. Two compounds with the same cationic ratio but different structures have been studied: cationic disordered La_{0.5}Ba_{0.5}CoO_{3- δ} with cubic symmetry and cationic ordered LaBaCo₂O_{6- δ} with tetragonal symmetry.

The cationic LaBaCo₂O_{6- δ} ordered phase shows lower strain values but a higher degree of anisotropy than the cationic La_{0.5}Ba_{0.5}CoO_{3- δ} disordered one. The minor degree of anisotropy for the cationic disordered phase was related to its cubic symmetry. The origin of the stress has been associated with the local order/disorder of La and Ba and the local concentration of oxygen vacancies, which produce a distribution of lattice parameters of the unit cell. Therefore, the minor strain in LaBaCo₂O_{6- δ} suggests that the distribution of cations in layers is structurally more favorable than cations randomly distributed.

NPD has allowed us to obtain precise information on the O sublattice and O-migration path. The oxygen vacancies of LaBaCo₂O_{6- δ} are mainly located in LaO layers. However, the O ions located in the CoO₂ layer are highly delocalized, contributing to the O-diffusion process. Rietveld refinement and bond valence sum methods suggest that O3 is more weakly bonded than the O1 and O2 O-atom sites in the LaBaCo₂O_{6- δ} structure and also than the O atoms in cubic La_{0.5}Ba_{0.5}CoO_{3- δ} . The atomic displacement and Fourier maps suggest a two-dimensional diffusional path for oxygen migration in LaBaCo₂O_{6- δ} , whereas this migration is isotropic along three dimensions in La_{0.5}Ba_{0.5}CoO_{3- δ} . The lowest dimensionality for the O-migration path harms the ionic conductivity in the tetragonal LaBaCo₂O_{6- δ} structure compared to the cubic La_{0.5}Ba_{0.5}CoO_{3- δ} .

Both LaBaCo₂O_{6- δ} and La_{0.5}Ba_{0.5}CoO_{3- δ} compounds exhibit high electrical conductivity values with a metallic like behavior. The combination of electrical conductivity with oxygen content data indicates that the conductivity mechanism is *via* electron-hole charge carriers. Two structural

features are detrimental to the electrical conductivity of the cationic ordered phase in contrast to La_{0.5}Ba_{0.5}CoO_{3- δ} :

(a) The two-dimensional instead of three-dimensional conductivity. This lower dimensionality for the electron-hole transport was associated with the blocking of the *c* direction owing to the existence of a high concentration of oxygen vacancies in the LaO layers.

(b) The loss of overlap between the Co 3*d* and O 2*p* orbitals, since the octahedral distortion enlarges the Co—O₂ distance and decreases the O₂—Co—O₂ angles.

This work was supported by CONICET, CNEA, ANPCyT and Fundación Balseiro from Argentina, through PICT 2010-0850 and PIP 11220080100120, and by Institut Laue–Langevin through ILL research proposal 47269. We also thank Professor N. Gonzalez and M. C. Ferreira from Balseiro Institute for their help in the English revision of the manuscript.

References

- Chen, Y., Yashima, M., Peña-Martínez, J. & Kilner, J. A. (2013). *Chem. Mater.* **25**, 2638–2641.
- Frontera, C., Caneiro, A., Carrillo, A. E., Oró-Solé, J. & García-Muñoz, J. L. (2005). *Chem. Mater.* **17**, 5439–5445.
- Hu, Y., Hernandez, O., Broux, T., Bahout, M., Hermet, J., Ottochian, A., Ritter, C., Geneste, G. & Dezanneau, G. (2012). *J. Mater. Chem.* **22**, 18744–18747.
- Ishihara, T., Fukui, S. & Nishiguchi, H. (2002). *Solid State Ionics*, **152–153**, 609–613.
- Itoh, T., Hirai, T., Yamashita, J., Watanabe, S., Kawata, E., Kitamura, N., Idemoto, Y. & Igawa, N. (2010). *Physica B*, **405**, 2091–2096.
- Itoh, T., Shirasaki, S., Fujie, Y., Kitamura, N., Idemoto, Y., Osaka, K., Hirose, I. & Igawa, N. (2009). *Electrochemistry*, **77**, 161–168.
- Kim, J.-H., Moggi, L., Prado, F., Caneiro, A., Alonso, J. A. & Manthiram, A. (2009). *J. Electrochem. Soc.* **156**, B1376–B1382.
- Kim, J., Prado, F. & Manthiram, A. (2008). *J. Electrochem. Soc.* **155**, B1023–B1028.
- McIntosh, S., Vente, J. F., Haije, W. G., Blank, D. H. A. & Bouwmeester, H. J. M. (2006). *Chem. Mater.* **18**, 2187–2193.
- Moggi, L. V., Prado, F. D., Cuello, G. J. & Caneiro, A. (2009). *Chem. Mater.* **21**, 2614–2623.
- Nakajima, T., Ichihara, M. & Ueda, Y. (2005). *J. Phys. Soc. Jpn.* **74**, 1572–1577.
- Pang, S. L., Jiang, X., Li, X., Su, Z., Xu, H., Xu, Q. & Chen, C. (2012). *Int. J. Hydrogen Energy*, **37**, 6836–6843.
- Pang, S., Jiang, X., Li, X., Wang, Q. & Su, Z. (2012). *Int. J. Hydrogen Energy*, **37**, 2157–2165.
- Pang, S. L., Li, X. N., Wang, Q. & Zhang, Q. Y. (2012). *Mater. Chem. Phys.* **131**, 642–645.
- Petric, A., Huang, P. & Tietz, F. (2000). *Solid State Ionics*, **135**, 719–725.
- Rautama, E., Boullay, P., Kundu, A. K., Caignaert, V., Pralong, V., Karppinen, M. & Raveau, B. (2008). *Chem. Mater.* **20**, 2742–2750.
- Rautama, E., Caignaert, V., Boullay, Ph., Kundu, A., Pralong, V., Karppinen, M., Ritter, C. & Raveau, B. (2009). *Chem. Mater.* **21**, 102–109.
- Rodríguez-Carvajal, J. (2000). *FullProf 2000*. Laboratoire Léon Brillouin (CEA-CNRS), Gif sur Yvette, France.
- Schmidt, M. & Campbell, S. (2002). *J. Phys. Chem. Solids*, **63**, 2085–2092.
- Sehlin, S., Anderson, H. & Sparlin, D. (1995). *Phys. Rev. B*, **52**, 11681–11689.
- Setevich, C., Moggi, L., Caneiro, A. & Prado, F. (2012). *J. Electrochem. Soc.* **159**, B73–B80.

- Stephens, P. W. (1999). *J. Appl. Cryst.* **32**, 281–289.
- Streule, S., Podlesnyak, A., Pomjakushina, E., Conder, K., Sheptyakov, D., Medarde, M. & Mesot, J. (2006b). *Physica B*, **378–380**, 539–540.
- Streule, S., Podlesnyak, A., Sheptyakov, D., Pomjakushina, E., Stingaciu, M., Conder, K., Medarde, M., Patrakeev, M. V. Leonidov, I. A., Kozhevnikov, V. L. & Mesot, J. (2006a). *Phys. Rev. B*, **73**, 094203.
- Suntsov, A., Leonidov, I., Patrakeev, M. & Kozhevnikov, V. (2011). *J. Solid State Chem.* **184**, 1951–1955.
- Tai, L., Nasrallah, M. M., Anderson, H. U., Sparlin, D. M. & Sehlin, S. R. (1995). *Solid State Ionics*, **86**, 273–783.
- Tarancón, A., Marrero-López, D., Peña-Martinez, J., Ruiz-Morales, J. C. & Nuñez, P. (2008). *Solid State Ionics*, **179**, 611–618.
- Tarancón, A., Skinner, S., Chater, R., Hernández-Ramírez, F. & Kilner, J. (2007). *J. Mater. Chem.* **17**, 3175–3181.
- Taskin, A. A., Lavrov, A. N. & Ando, Y. (2005). *Appl. Phys. Lett.* **86**, 091910.
- Teraoka, Y., Zhang, H., Okamoto, K. & Yamazoe, N. (1988). *Mater. Res. Bull.* **23**, 51–58.
- Zhang, K., Ge, L., Ran, R., Shao, Z. & Liu, S. (2008). *Acta Mater.* **56**, 4876–4889.
- Zhou, W., Ran, R. & Shao, Z. (2009). *J. Power Sources*, **192**, 231–246.